Solid Earth Discuss., 7, 1399–1446, 2015
www.solid-earth-discuss.net/7/1399/2015/
doi:10.5194/sed-7-1399-2015

Solid Earth Discussions
Open Access

Strain localization in brittle-ductile shear zones: fluid abundant vs fluid limited conditions (an example from Wyangala area, Australia)

L. Spruzeniece and S. Piazolo

Australian Research Council Centre of Excellence for Core to Crust Fluid Systems/GEMOC, Department of Earth and Planetary Sciences, Macquarie University, NSW, Australia

Received: 10 March 2015 – Accepted: 17 March 2015 – Published: 17 April 2015

Correspondence to: L. Spruzeniece (liene.spruzeniece@mq.edu.au)

Published by Copernicus Publications on behalf of the European Geosciences Union.

Abstract

This study focuses on physiochemical processes occurring in a brittle-ductile shear zone at both fluid-present and fluid-limited conditions. In the studied shear zone (Wyangala, SE Australia), a coarse-grained two feldspar-quartz-biotite granite is transformed into a medium grained orthogneiss at the shear zone margins and a fine-grained quartz-muscovite phyllonite in the central parts. The orthogneiss displays cataclasis of feldspar and crystal-plastic deformation of quartz. Quartz accommodates most of the deformation and is extensively recrystallized showing distinct crystallographic preferred orientation (CPO). Feldspar-to-muscovite, biotite-to-muscovite and albitization reactions occur locally at porphyroclasts' fracture surfaces and margins. However, the bulk rock composition shows very little change in respect to the wall rock composition.

In contrast, in the shear zone centre quartz occurs as large, weakly deformed porphyroclasts, in sizes similar to that in the wall rock, suggesting that it has undergone little deformation. Feldspars and biotite are almost completely reacted to muscovite, which is arranged in a fine-grained interconnected matrix. Muscovite-rich layers contain significant amounts of fine-grained intermixed quartz with random CPO. These domains are interpreted to have accommodated most of the strain. Bulk rock chemistry data shows a significant increase in SiO_2 and depletion in NaO content compared to the wall rock composition.

We suggest that the high and low strain fabrics represent markedly different scenarios and cannot be interpreted as a simple sequential development with respect to strain. We suggest that the fabrics and mineralogical changes in the shear zone centre have formed due to fluid influx probably along an initially brittle fracture. Here, hydration reactions dramatically changed the rheological properties of the rock. In the newly produced muscovite-quartz layers creep cavitation associated with grain boundary sliding and fluid pumping resulted in strain localization, further fluid influx and subsequent substantial changes in bulk chemistry. Strain partitioning between the "soft" muscovite-quartz layers and "hard" original igneous quartz grains allows preservation of the ig-

SED

7, 1399–1446, 2015

neous quartz grains. In contrast, in the shear zone margins the amount of fluid and reactions was limited; here deformation was mainly accommodated by recrystallization of the igneous quartz grains.

The studied shear zone exemplifies the role of syn-deformational fluids and fluid-induced reactions on the dominance of deformation processes and subsequent contrasting rheological behaviour at micron- to meter scale.

1 Introduction

The brittle-ductile transition zone (BDTZ) represents the strongest part of the Earth's crust (Kohlstedt et al., 1995), the main seismogenic layer (e.g. Sibson, 1982; Scholz, 2007) and is a major source and transport region for ore-forming fluids (e.g. Kolb et al., 2004). However it is also the least understood part of the continental crust, where the rheological strength estimates and assumptions of rock deformation mechanisms vary widely.

BDTZ is defined as a transitional layer between the pressure-dependent brittle rheology of the upper crust and thermally activated viscous creep in the lower crust (Handy et al., 2007). Highly localized shear zones control the deformation at this depth. The strength of BDTZ is commonly estimated using power-law rheology of quartz, which is the weakest and most abundant phase in granitic assemblages. Experimental data demonstrate that power-law creep in quartz can be activated at temperatures as low as 300 °C, while feldspar, being another abundant mineral in granitoids, has a high frictional strength up to the temperatures of 500 °C (Passchier and Trouw, 2005).

However, in nature brittle-ductile shear zones are often found to be altered by syn-tectonic fluids (Hippertt, 1998; Goncalves et al., 2012; Wintsch and Yeh, 2013; Oliot et al., 2014). The chemical and physical consequences of fluid-rock interaction have been subject of many studies demonstrating the major effects fluid introduces on rock rheology. Infiltration of pressurized fluid can cause brittle failure even at high confining pressures (Byerlee, 1990) allowing frictional deformation at high temperatures and

SED
7, 1399–1446, 2015

low differential stresses. An increasing number of field studies recognize fluid-induced brittle precursors as the main cause for shear zone nucleation in the middle crust (Fusseis and Handy, 2008; Menegon et al., 2008; Menegon and Pennacchioni, 2010; Kilian et al., 2011; Brander et al., 2012). The fluid presence in brittle-ductile shear zones is typically associated with a variety of weakening mechanisms: (1) chemical breakdown of feldspars into weak hydrous minerals (White and Knipe, 1978; Hippertt, 1998; Oliot et al., 2014); (2) reaction-controlled grain size reduction by growth of fine-grained metasomatic assemblages (White and Knipe, 1978; Kilian et al., 2011); (3) switch of the dominant deformation mechanisms from solid state power-law rheology to fluid facilitated Newtonian flow (Menegon et al., 2008; Wintsch and Yi, 2002; Brander et al., 2012), (4) hydrolytic weakening in minerals deforming by crystal-plastic mechanisms (Tullis and Yund, 1980; Karato et al., 1986). Based on these observations the strength of the BDTZ is suspected to be orders of magnitude lower comparing to the estimates from the quartz-based rheology (Bos and Spiers, 2002; Mariani et al., 2006; Park et al., 2006; Marsh et al., 2009) where the particular role and contribution of each weakening mechanism is still under a debate.

Fluid transit through BDTZ requires fluid pathways within the mylonitic microstructure. As pointed out by Mancktelow (2006), the fact that fluid flows into and along the shear zones rather than being expelled requires a brittle component and local pressure drops during deformation. This conclusion has led to a concept of a dynamic porosity suspected to exist even at high lithostatic pressures. The recent work by Fusseis and collaborators (Fusseis et al., 2009; Menegon et al., 2015) highlights the importance of deformation in maintaining fluid pathways in the crust. At the same time, a recent study by Billia et al. (2013) suggests high permeability within a brittle-ductile shear zone fabric.

In many cases the difference between fluid-abundant and fluid-limited/absent conditions is difficult to assess in natural shear zones. Often only one of the two scenarios is preserved. This study takes advantage of the occurrence of fluid-facilitated and fluid-restricted deformation within the same brittle-ductile shear zone providing the possibil-

SED
7, 1399–1446, 2015

ity to discern the particular microstructural changes and rheological effects caused by syn-tectonic fluids. Results demonstrate the microstructural and rheological difference in each case and reveals the interplay between the dynamics of fluid flux, deformation mechanism and strain localization within the middle crust.

2 Geological setting

2.1 Regional geology

The studied shear zone is one of the Wyangala shear zones, which is developed within the Wyangala batholith, situated in the Eastern Lachlan Fold belt (Fig. 1), one of the three structural regions in the Lachlan Orogen, SE Australia (Gray, 1997). The Eastern Lachlan Fold belt consists of voluminous granitic to granodioritic plutons and mafic volcanics, quartz-rich turbidites, carbonates and shales (Vandenberg and Stewart, 1992). The regional tectonic reconstructions suggest that the Lachlan orogeny formed during an accretion of a volcanic island arc along the eastern margin of Gondwana from about 450 to 340 Ma with a deposition of turbidite complexes and volcanics in a back-arc or a forarc basin during a rifting phase in Ordovician (Foster et al., 2009).

Regionally the Eastern Lachlan subprovince displays a characteristic N–S trending, eastward dipping fault-thrust systems (Glen, 1992; Gray, 1997). The plutons are aligned parallel to this structural grain and often associate with the fault system. The observation of narrow contact aureoles in the host rock and undeformed margins of the plutons are considered to support a passive emplacement along pre-existing fault planes (Paterson et al., 1990; Paterson and Tobisch, 1992). The crystallization ages of the plutons in the Eastern Lachlan province are estimated from geochronological studies and show a range between 435 and 425 Ma (Lennox et al., 2005; Squire and Crawford, 2007). Recent zircon SHRIMP U-Pb study by Lennox et al. (2014) dates the crystallization of the Wyangala granite as Late Silurian (425.2 ± 3.5 Ma).

SED
7, 1399–1446, 2015

Overprinting the major fault systems, smaller scale shear zones are seen along the eastern margins of the granitic plutons. They are westward-dipping, generally N–S trending and indicate west-over-east sense of shear (Paterson et al., 1990). The Wyangala shear zone system belongs to one of such structures, located on the eastern margin of the Wyangala Granite. The main shearing event in these shear zones has been dated by Ar/Ar method using recrystallized K-feldspar (Lennox et al., 2014) to 375–365 Ma corresponding to the late Devonian Tabberabberan deformation event.

2.2 Outcrop and general sample description

The study area is located within the Wyangala shear zone system in the vicinity of Wyangala Dam about 25 km SE of Cowra, NSW (33°56.855′ S and 148°57.982′ E; Fig. 1). The outcrop exposes a weakly to strongly deformed granitic massif. The wall rock is a weakly foliated monzogranite with up to 8 cm large feldspar phenocrysts, quartz filling the interstices and biotite marking the incipient, discontinuous foliation planes (Fig. 2c).

Based on the structural and mineralogical properties we distinguish 2 domains within the studied shear zone: (1) orthogneiss in the shear zone margins and (2) phyllonite in the central part. The transition from the wall rock into orthogneiss occurs over a 0.5–1 m distance, characterized by a gradual decrease in grain sizes and a development of a thin-spaced, continuous foliation, defined by phyllosilicates. Feldspar grains become more fragmented towards the shear zone centre and quartz is more and more arranged in elongated lenses or layers (Fig. 2a and c).

The boundary between the orthogneiss and phyllonite is sharp and marked by a sudden strengthening of foliation and disappearance of feldspar grains (Fig. 2a and c). The central domains display centimetre- to millimetre-scale alteration between two types of phyllonites (Fig. 2b). Phyllonite A is composed of fine, muscovite-dominated matrix surrounding large, elongated quartz grains. These large quartz grains in phyllonite A have similar sizes to quartz in the wall rock. Phyllonite B contains more quartz than phyllonite A, but have a larger matrix mode and exhibits higher phase mixing (Fig. 2c).

SED
7, 1399–1446, 2015

In total 9 samples were collected from all distinguished lithologies, representing wall rock, orthogneiss and both types of phyllonite.

3 Methods

3.1 Sample selection and preparation

Samples were cut perpendicular to the foliation (YZ plane) and parallel to the stretching lineation (X axis) and polished down to ~ 30 µm thickness for thin sections. In total 16 thin sections were prepared for detailed optical and chemical analysis. For Electron Backscatter Diffraction (EBSD) analysis a colloidal silica–water solution (mixed in proportion 80 : 20) was used at the final stage of polishing for 3–5 min to reduce surface damage produced by mechanical polishing. All thin sections were carbon-coated for Scanning Electron Microscopy (SEM) analysis.

In order to ensure comparability, all quantitative analysis, including XRF, EBSD, point counting and image analysis were carried out on the same 4 selected samples, representing each shear zone domain (W17 – wall rock; W13b – orthogneiss; W21b – phyllonite A; W21c – phyllonite B). Their locations are given in Fig. 2a, b.

The mineral abbreviations used in the following sections follow the recommendations of Kretz (1983).

3.2 Mineral chemistry

Overall characterization of the rock forming minerals, and chemical composition of plagioclase were determined using Energy Dispersive Spectrometry (EDS) on a Carl Zeiss IVO SEM at the Geochemical Analysis Unit (GAU, Macquarie University), using AzTec analysing software from Oxford Instruments. The analytical accuracy of anhydrous phases, such as feldspars is 0.1 to 0.2 wt. %. The analyses were performed at high vacuum conditions with an accelerating voltage of 15–20 kV, a beam current of 5.0–10.0 nA at working distances from 12 to 12.5 mm.

SED
7, 1399–1446, 2015

3.3 Orientation analysis and data processing

Crystallographic orientation data were acquired using HKL NordlysNano high sensitivity Electron Backscatter Diffraction (EBSD) detector and indexed with AzTec analysis software (Oxford Instruments) at the Geochemical Analysis Unit (GAU, Macquarie University). The analyses were carried out on a sample tilted to 70° angle, in high vacuum conditions with 20 kV accelerating voltage and a beam current of 8.2 nA, at working distances from 9–13 mm. The typical step sizes ranged from 1–5 µm, depending on the required resolution and the average grain size in the region of interest. Simultaneously with EBSD data, EDS data were collected to assist with the phase determination during post-processing of the acquired data.

Channel 5 analysis software from HKL Technology was used for the post-acquisition processing of the stored EBSD patterns. The obtained EBSD maps contained from 5 to 26 % of non-indexed points (zero solutions), mostly resulting from the difficulty to index phyllosilicates. The map quality was first improved by a "standard" noise reduction following the procedure of Prior et al. (2002) and Bestmann and Prior (2003). The second step included the removal of "fake grains" (all grains with area, smaller than a squared step size), where grains were determined by a minimum grain boundary angle of 10° and subgrains were defined by a boundary angle of 2–10° in intra-grain regions. After the processing procedure, indexing in all maps except of one exceeded 80 %, and was close to 100 % for quartz-dominated mineralogies.

Pole figures were calculated using one point per grain, and plotted on the upper hemisphere equal area projections with stretching lineation parallel to X axis and foliation normal to Z axis. All maps and datasets were rotated consistent with a dextral shear sense as determined by asymmetry of quartz orientations. No unequivocal shear sense indicators were found on field. In field it was not possible to determine shear sense unequivocally.

SED
7, 1399–1446, 2015

3.4 Modal composition

The modal amounts of mineral phases (Fig. 3a) were determined using point counting method for the four representative thin sections. As a minimum 1000 points for each thin section were counted. Modal amounts of quartz microstructures (Fig. 3b) were estimated on the same four thin sections using manually outlined optical micrographs and the imaging software Image J (http://imagej.nih.gov/ij/index.html). As one quartz microstructure (Qtz_3; details in the following) is very fine-grained and occurs in mixtures with muscovite, it could not be quantified directly, and thus was estimated by subtracting the sum of the other two quartz microstructure modes ($Qtz_1 + Qtz_2$) from the total quartz mode determined by point counting.

3.5 Whole-rock analysis

Bulk whole rock major-, minor- and trace element concentrations were measured by X-ray fluorescence (XRF) analysis for the four chosen representative samples from each shear zone domain (Fig. 2a). Samples were processed into fine powders and analysed with a PANalytical PW2400 Sequential WDXRF Spectrometer at the University of New South Wales. Obtained datasets are presented in Table 1.

3.6 Isocon method

To quantitatively evaluate the mass transfer between the shear zone domains we used isocon method by Grant (1986) based on the composition-volume equations proposed by Gresens (1967). It allows to estimate the absolute change in the concentration for each individual oxide using equation:

$$\Delta M_j = \left(\left(\frac{C_i^p}{C_i^a} \right) \left(\frac{C_j^a}{C_j^p} \right) - 1 \right) \times 100, \quad (1)$$

SED
7, 1399–1446, 2015

where ΔM is the mass change in percents; (C) – concentration; superscripts (p) and (a) stands for protolith and altered sample; subscripts (i) and (j) stands for immobile and mobile elements.

The slope of the isocon ($S = \left(C_i^a / C_i^p\right)$ reflects the total mass difference between each two analysed samples. The absolute change in total mass (in %) thus was estimated using the equation:

$$\Delta M_{total} = \left(\left(\frac{1}{S}\right) - 1\right) \times 100 \quad (2)$$

For the isocon construction and calculations we assumed the immobility of aluminium (Al_2O_3) as (i) it has been shown to be immobile during the deformation of granitoids in greenschist facies shear zones (Eilu et al., 2001; Rolland et al., 2003) and (ii) it is consistent with microstructural observations in the studied samples.

4 Results

4.1 Optical microstructures, phase abundance and mineral chemistry

4.1.1 Wall rock: weakly foliated monzogranite

The wall rock consists of 34 % quartz, 25 % plagioclase, 21 % K-feldspar, 14 % biotite, 5 % muscovite and < 1 % accessory minerals (zoesite, apatite, chlorite, zircons and Fe-Ti oxides) (Fig. 3a).

The most typical quartz microstructure in the wall rock, further referred as Qtz_1 (Figs. 3b and 4) is characterized by up to 5 mm long grains with anhedral, equidimensional or slightly elongated shapes having aspect ratios of ~ 1 to 1.5. Intracrystalline deformation features such as undulose extinction and deformation lamellae are common in these grains, subgrains occur occasionally. Quartz additionally occurs as fine-grained, largely monocrystalline aggregates associating with Qtz_1 grains (Fig. 4a).

SED
7, 1399–1446, 2015

These microstructures are referred to in the following as Qtz_2. In the wall rock Qtz_2 constitute only a minor amount (Fig. 3b).

Plagioclase and K-feldspar in the wall rock typically occur as 5–8 mm large, euhedral or subhedral grains, referred as Pl_1 and Kfs_1, respectively (Fig. 4). Pl_1 displays normal compositional zoning characterized by Ca-enriched cores ($ab_{59–81}$) and Na-rich rims ($ab_{92–94}$). The cores are heavily altered to fine-grained muscovite, K-feldspar and epidote, while the rims rarely contain inclusions. Intergrown clusters of two or three Pl_1 grains are common. Euhedral Pl_1 grains occasionally occur in the interiors of larger Kfs_1 grains. All Kfs_1 ($or_{96–100}$) are perthitic with albite ($ab_{96–98}$) lamellae covering about 20 % of the grain area (Fig. 4b and c). These grains often exhibit fragmentation and pull-apart fractures filled with fibrous or blocky quartz and biotite, but do not display significant displacement in respect to each other.

Biotite (Bt_1) is the dominant phyllosilicate in the wall rock assemblage (Fig. 3a) and occurs as up to 5 mm long grains (Fig. 4a). Rare, up to 3 mm long muscovite (Ms_1) grains can also be seen in the wall rock (Fig. 4c). Typically phyllosilicates display well-developed cleavage and minor kinking and fracturing. Apatite and zircon occur as inclusions in Bt_1 grains.

4.1.2 Shear zone margin: orthogneiss

The orthogneiss is composed of 46 % quartz, 18 % muscovite, 13 % plagioclase, 11 % K-feldspar, 7 % biotite and 5 % epidote (Fig. 3a).

Up to 70 % of quartz in this domain (Fig. 3b) is represented by the fine-grained Qtz_2 aggregates (Fig. 5a, c and f). The average size of Qtz_2 grains is between 15–25 µm, the grains have aspect ratio of about 1.8 and display a shape preferred orientation (SPO). Qtz_1-type grains are rare (~ 8 % of all quartz) and commonly surrounded by mantles of Qtz_2 aggregates. Qtz_1 is typically up to 1 cm long, with aspect ratios between 3 and 4, and displays undulose extinction, subgrains, slightly serrated boundaries and intragranular bands and patches of Qtz_2 aggregates (Fig. 5a and f). Another quartz microstructure referred to in the following as Qtz_3 can be distinguished in the

SED
7, 1399–1446, 2015

orthogneiss (Fig. 3b). It is characterized by very fine grain sizes and often intermixed with fine-grained muscovite (Fig. 5a, d and e). Here, it is mainly seen in strain shadows of feldspar grains.

Both, plagioclase and K-feldspar form up to about 3 mm long grains with aspect ratios of 1.5–1.8. Due to the microstructural and chemical similarity with feldspars in the wall rock, we refer to them as Pl_1 and Kfs_1. Both, Pl_1 and Kfs_1, occur in association with fine-grained muscovite (Ms_2) mantles (Fig. 5a–e). While Pl_1 grains tend to have rounded and irregular shapes, Kfs_1 forms clusters of angular grains and display intragranular fractures, rotated fragments, bookshelf structures and pull-aparts. The fractures and strain shadows of feldspar grains are filled with a non-pertitic K-feldspar, further referred as Kfs_2, fine-grained albitic plagioclase ($ab_{95–99}$), referred as Pl_2, fine-grained quartz (Qtz_3) and muscovite (Ms_2) mixtures (Fig. 5d and e).

Phyllosilicates in the orthogneiss are mostly represented by Ms_2 (Fig. 3a). Biotite and epidote are commonly present in the Ms_2-rich bands but do not have a direct contact with feldspar grains.

4.1.3 Shear zone centre: Phyllonite A

The mineralogy of the phyllonite A is dominated by quartz (62 %), muscovite (25 %) and epidote (11 %), with minor amounts of plagioclase (~ 1.7 %) and biotite (~ 1.4 %) (Fig. 3a).

Qtz_1 grains are larger than in the orthogneiss, approaching sizes comparable to Qtz_1 in the wall rock (Fig. 6a). They are typically elongated with aspect ratios close to 4 and length up to 8 mm. Intracrystalline deformation structures, including undulose extinction, subgrains and deformation lamellae are common. Fine-grained aggregates of Ms_2, Qtz_3, Ep_2 and Pl_2 form thick layers around Qtz_1 grains. In some parts this matrix can consist of up to 70 % of very fine Qtz_3-type grains with average grain sizes of about 5–8 µm and aspect ratios of 1.8–1.9. The tails of Qtz_1 grains commonly consist of mixtures of fiber-shaped Qtz_3-Ms_2 (Fig. 6d).

SED
7, 1399–1446, 2015

Qtz_2 aggregates in the phyllonite A constitute only 13 % of the total quartz mode, in contrast to the high abundances in the orthogneiss (Fig. 3b). They show similar relationship to Qtz_1 grains as in orthogneiss, but do not form thick mantles.

Feldspars are represented by up to 1 mm large Na-rich ($ab_{97–100}$) plagioclase (Pl_2) grains (Fig. 6a and c). They are commonly surrounded by Ms_2-rich matrix and epidote clusters and display a well-pronounced, parallel fracture sets filled by Ms_2. Some of the Pl_2 grains are twinned and have undulose extinction.

4.1.4 Shear zone centre: phyllonite B

Samples from phyllonite B are mainly composed of quartz (83 %) and muscovite (15 %); with small amounts of epidote (~ 1.5 %), biotite (~ 0.3 %) and minor plagioclase (~ 0.1 %) (Fig. 3a).

The microstructure in phyllonite B consists of cm- to mm-scale alternating bands of mixed, fine-grained aggregates of Qtz_3-Ms_2. Variations in the modal amounts of the two phases characterize the layering (Fig. 6b and g). All muscovite is referred as Ms_2, due to the similarity with Ms_2 microstructure in orthogneiss and phyllonite A. The grains are typically 10–20 µm in length and aligned subparallel to the main foliation. Muscovite-poor layers display typical Qtz_1-Qtz_2 associations, similar to the ones in orthogneiss, with elongated up to 5 mm long Qtz_1 grains in the central parts, surrounded by mantles of fine-grained Qtz_2. In domains, rich in muscovite very fine-grained Qtz_3 is homogenously intermixed with fine-grained Ms_2. The grain size of Qtz_3 depends of the Ms_2 amount present (Fig. 6g). It varies from 8 µm in domains with 30 % muscovite to 20 µm in domains with 5 % Ms_2.

4.2 Crystallographic orientation analysis

Crystallographic preferred orientation (CPO) analysis focuses on quartz microstructure. No EBSD analysis is necessary for muscovite, which exhibits a well pronounced SPO that can be directly linked to its CPO as the basal slip plane in muscovite is parallel

SED
7, 1399–1446, 2015

to the SPO. Feldspars show dominantly brittle deformation, thus no specific crystallographic orientation data was sought for these. In the following, we characterize in detail the different quartz types as identified from optical analysis.

4.2.1 Qtz_1 porphyroclasts

Figure 7b shows a combined pole plot for six Qtz_1-type grains from all deformed shear zone domains. The bulk orientation of these grains is non-random, with the poles of *c* axis clustering 5–45° clockwise from *Z* direction. This arrangement is consistent with the general shear sense in the analysed samples. In the second pole figure (Fig. 7b), a CPO pattern of a single strongly deformed Qtz_1 grain is presented showing the range of internal deformation in the crystal lattice. Two *c* axis maxima appears next to the opposite poles of *Z* direction, lying on the same great circle.

Internally Qtz_1 grains show a high degree of lattice distortions, with high abundance of subgrain boundaries, most of them oriented approximately in 45° angles to the foliation plane (Fig. 7a). The variations of internal misorientation across a single grain can reach more than 40° (Fig. 7c; profile 1). Dauphine twin boundaries, identified by the $60 \pm 2°$ lattice rotation around the *c* axis, are common (Fig. 7a). They typically occur as irregular patches in highly deformed internal parts or along highly stressed edges of the grains.

4.2.2 Qtz_2 aggregates

Grain orientations in the fine-grained Qtz_2 domains always display a strong CPO. In the surroundings of Qtz_1 porphyroclasts, the CPO of Qtz_2 grains tend to cluster close to the porphyroclast orientation with a slight rotation towards the centre of the pole figure (Fig. 8b; map 1). In the homogenous Qtz_2 domains, devoid of Qtz_1 grains, the CPO of Qtz_2 is arranged in an asymmetric Type Ia crossed-girdle pattern (Passchier and Trouw, 2005), subparallel to *Z* direction and synthetic with the shear direction (Fig. 8b; map 2).

SED
7, 1399–1446, 2015

Subgrain and Dauphine twin boundaries are common (Fig. 8a). The variations in internal misorientation angles across single grains typically range from 2 to 4°, but can reach up to 9° misorientation in the largest grains (Fig. 8c).

4.2.3 Qtz_3 in muscovite-quartz mixtures

Two associations of Qtz_3 grains were analysed in phyllonite A and phyllonite B; one from a tail of a Qtz_1-type grain, another from an interior of a fine-grained quartz-muscovite band (Figs. 6a and 9a). The crystallographic orientation of Qtz_3 grains at the tails of Qtz_1, typically clusters close to the orientation of the Qtz_1 grain (Fig. 9b; map 1). Often the Qtz_3 grains in these tails form string-like aggregates. Misorientation profiles across individual grains parallel to the elongation of these "strings" do not exceed 15° between adjacent grains (Fig. 9c; profile 1).

In contrast, Qtz_3 grains in the matrix-forming Qtz-Ms bands display close to random CPO (Fig. 9b; map 2ii). Domains with smaller muscovite content may have similar, or slightly larger grain sizes but show much stronger CPO than muscovite-rich domains (Fig. 9b, map 2i vs. map 2ii). Despite of the small grain size (average 8 µm) the individual Qtz_3 grains display subgrains, Dauphine twinning and lattice bending, typically ranging from 1 to 3°, but angles even up to 13° are not uncommon (Fig. 9c; profile 2).

4.3 Whole rock geochemistry

Figure 10a shows that the chemical composition of the orthogneiss closely resembles the composition of the wall rock. The slope of the isocon approximates 1 and all the major elements lay near to the isocon. Slight enrichment in CaO and depletion in Mn_3O_4, MgO, P_2O_5 and K_2O may be related to the heterogeneity of the analysed samples.

The element concentrations in phyllonite A deviate from the isocon more significantly (Fig. 10b; Table 1). The SiO_2 and FeO show enrichment in the concentration, reflecting the increased quartz and epidote modes in the phyllonite A (Fig. 3a). But all the other major elements, especially Na_2O are depleted. The major loss in Na_2O (−79 %)

SED
7, 1399–1446, 2015

coincides with the decrease in feldspar mode from 46 % in the wall rock to 1.7 % in phyllonite *A* (Fig. 3a). Furthermore, the isocon itself lies below the "constant mass" line (dashed line in Fig. 10) indicating a total mass increase of 12.2 % comparing to the wall rock domain.

Phyllonite B maintains the chemical trends displayed by phyllonite *A*, but shows more extreme deviations from the wall rock composition (Fig. 10c; Table 1). The isocon slope of 0.29 equates to a total mass gain of 239 %. Large gains in SiO_2 (+332 %) concentration correspond to the increase in quartz mode from 34 % in the wall rock to 83 % in the phyllonite B (Fig. 3a). Na_2O again shows depletion, approaching concentration close to 0, which reflects the loss of feldspars in the shear zone centre.

5 Discussion

5.1 Orthogneiss and phyllonite: same protolith, or not?

The studied shear zone displays two mineralogically and structurally different domains: (1) marginal domains containing orthogneiss, similar in composition to the wall rock, and (2) central domains with a muscovite-quartz phyllonite exhibiting a significant change in bulk chemistry. An important question regarding the interpretation of the shear zone microstructures and its formation is whether both of these domains originated from the same protolith; or represent pre-existing heterogeneities in the wall rock, such as dykes, veins or compositional layering.

In case of the orthogneiss, the interpretation of its origin is straightforward. The mineralogical and chemical similarity with the wall rock and the gradual microstructural change over a broad transition zone clearly implies a wall rock-type protolith. In contrast, the origin of very different chemical and microstructural characteristics in the central phyllonites, as well as the sharp interface with the marginal domains is more ambiguous to interpret. Several pieces of evidence however point to a metasomatic origin of these features, rather than a different protolith: (1) the incomplete hydration

SED
7, 1399–1446, 2015

reactions, asymmetric reaction rims, veins and fringes in orthogneiss indicate a presence of metasomatic fluids during the deformation (Fig. 5); (2) the mineralogy in the shear zone centre consist of reaction products observed in arrested replacement relationship in the marginal domains, (3) the trends of depletion or enrichment of major elements are gradual and generally consistent across the shear zone (Fig. 10).

Based on this evidence we suggest that mineralogy and microstructure in all shear zone domains is a result of syn-tectonic metasomatic alteration.

5.2 Mineral reactions and mass transfer

5.2.1 Orthogneiss: reactions and local mass transfer in a closed, fluid limited system

The mineralogical composition of the orthogneiss differs from the wall rock by increased modes of muscovite, quartz and epidote; and decreased amounts of feldspar and biotite (Fig. 3a).

The new metasomatic muscovite (Ms_2) occurs as fine-grained aggregates, aligned subparallel to the foliation fabric. Ms_2 is always in close spatial association with the igneous feldspars (Pl_1 and Kfs_1) and biotite (Bt_1). Both, Kfs_1 and Pl_1, display muscovite filled fractures and concave boundaries with fine-grained muscovite aggregates (Fig. 5b–e). Plagioclase, more often than K-feldspar, is surrounded by fine-grained muscovite-epidote mantles. Reactions responsible for these fabrics can be written as:

$$3KAlSi_3O_8 + 2H_2O \rightarrow KAl_3Si_3O_{10}(OH)_2 + 6SiO_2 + 2K^+ + 2OH^- \quad \text{(R1)}$$

and

$$4Ca_{0.2}Na_{0.8}Al_{1.5}Si_{2.5}O_8 + 0.8H_2O + 0.6K^+ + 0.2Fe^+ + 2.6SiO_2 \rightarrow$$
$$3.2NaAlSi_3O_8 + 0.6KAl_3Si_3O_{10}(OH)_2 + 0.4Ca_2Fe_{0.5}Al_{2.5}(SiO_4)_3(OH), \quad \text{(R2)}$$

where small amounts of pore fluid, probably provided by a deformation-facilitated breakdown of igneous biotite (Bt_1) and muscovite (Ms_1), interacts with the metastable

SED
7, 1399–1446, 2015

igneous feldspars. As a result Kfs_1 (reaction R1) breaks down to form muscovite, releasing silica and K^+ in the solution, both of which together with small amounts of Fe^+ can be further incorporated in the reaction R2, where igneous plagioclase of andesitic composition (Pl_1) breaks down to form albitic feldspar Pl_2, muscovite (Ms_2) and epidote (Ep_2). Both reactions requires grain-scale transport of K^+, confirming its mobility in the pore fluid, as already indicated by the occurrence of non-perthitic K-feldspar (Kfs_2) grains in pressure shadows and extensional sites around porphyroclasts (Fig. 5d and e). The lack of exsolution lamellae in this "new" Kfs_2, indicate the immiscibility of K^+ and Na^+ at the conditions of alteration. The Ca-content in Pl_1 promotes the formation of epidote (Ep_2). The excess Fe^+, necessary for Ep_2 production is possibly released from Bt_1, which is also seen to break down to Ms_2. Quartz, released in reaction R1 is not seen to intermix with muscovite but rather precipitate in strain shadows and fractures (Fig. 5e), suggesting high mobility of silica in the circulating fluid.

Indications of Na^+ mobility in fluid come from the observations of albitic rims and veinlets associating with Kfs_1 and can be described by a simple exchange reaction:

$$KAlSi_3O_8 + Na^+ \rightarrow NaAlSi_3O_8 + K^+, \quad \text{(R3)}$$

possibly governed by interface-coupled dissolution-precipitation processes (Putnis, 2009), as fluid phase must participate in the reaction as a transport medium for Na^+ and K^+, as they are not always available from the surrounding phases (Fig. 5d).

In summary, the microstructures in orthogneiss suggest the metastability of the wall rock assemblage during the deformation. The major reactions are feldspar-to-muscovite and biotite-to-muscovite breakdown, albitisation of feldspars and growth of metasomatic K-feldspar (Kfs_2), albite (Pl_2), epidote (Ep_2) and quartz (Qtz_3) indicating a local mobility of K^+, Na^+, Ca^+, Fe^+ and Si^+. However, the bulk rock composition of orthogneiss is highly similar to the wall rock composition (Fig. 10a) excluding a possibility of a large-scale mass transfer during the alteration. A minor amount of free fluid is required to enable reaction R1 and reaction R2 to occur and to facilitate the transport for components in all described reactions. Thus, the reactions in orthogneiss are best

SED
7, 1399–1446, 2015

explained by limited fluid influx and dominance of local element "recycling" in a "closed system" conditions, where mass transfer did not exceeded distances of mm to cm.

5.2.2 Phyllonite A and *B*: reactions and mass transfer in an open, fluid abundant system

Both phyllonites display dramatic changes in mineral and chemical composition with respect to the wall rock (Fig. 10b and c). Mineralogically, the differences include almost complete loss of K-feldspar, plagioclase and biotite, as well as increase in muscovite, quartz and epidote (Fig. 3a) content.

No igneous K-feldspar (Kfs_1) or plagioclase (Pl_1) remnants were observed in phyllonites, but the rare albite grains (Pl_2) typically associating with muscovite-quartz-epidote mantles, can be either products of the breakdown reactions of Pl_1; with Pl_2, Ms_2, Ep_2 and Qtz_3 as reaction products (reaction R2) or a result of an arrested/incomplete breakdown of Pl_2:

$$3NaAlSi_3O_8 + 2H^+ + K^+ \rightarrow KAl_3Si_3O_{10}(OH)_2 + 6SiO_2 + 3Na^+, \quad \text{(R4)}$$

resulting in the production of muscovite (Ms_2) and quartz (Qtz_3) and the release of Na^+ in the pore-fluid.

Although in some cases, reaction R2 may be operating, R4 is necessary to explain the eventual disappearance of albite and the general trend of Na^+ depletion indicated by the XRF data (Fig. 10b and c).

Both domains in the central part of the shear zone indicate net mass gains, mainly due to the increased Si^+ concentration. The modal analysis also shows the increase in the quartz content in both domains, suggesting external influx of Si^+ fluids. No loss of Si^+ is observed in the adjacent orthogneiss, excluding the possibility of a lateral transport.

In summary, the chemical reactions described in this section requires "open system" conditions with an influx of external Si^+-rich hydrous fluid, undersaturated in Na^+.

SED
7, 1399–1446, 2015

5.3 Deformation mechanisms and strain localization

5.3.1 Shear zone margins: orthogneiss

Deformation in shear zone margins mainly occurs by crystal-plastic and cataclastic processes where ductile deformation is focussed in quartz while feldspar deforms in a brittle manner.

The larger Qtz_1 grains, representing porphyroclastic remnants of the igneous quartz show abundance of undulose extinction, deformation lamellae and subgrain boundaries indicating operation of dislocation creep processes (White, 1967; Poirier, 1980; Urai et al., 1986). The finer grained Qtz_2, often surrounding porphyroclasts (Qtz_1), have similar sizes and shapes to the subgrains suggesting formation by subgrain rotation (SGR) recrystallization. The presence of serrated grain boundaries suggests a component of bulging (BLG) recrystallization involving low temperature grain boundary migration (Hirth and Tullis, 1992), where bulging may have been partly facilitated by intergranular fluids (Mancktelow and Pennacchioni, 2004). The fact that Qtz_2, further interpreted as the recrystallized fraction in the orthogneiss, represent close to 70 % of the orthogneiss and forms interconnected, fine-grained layers suggests low rheological strength of quartz and significance of crystal-plastic processes.

The combined EBSD data for all analysed Qtz_1 grains shows *c* axes lying synthetically oblique to the shear direction. This pattern has been previously documented by (Menegon et al., 2011) and interpreted as a selective preservation of only those grains, which are optimally oriented for a slip on basal plane.

The CPO of the recrystallized Qtz_2 grains either cluster around the orientation of the adjacent porphyroclast (Fig. 8b; map 1) reflecting a "parent"-controlled misorientation relationship during a progressive subgrain rotation (Kruse et al., 2001; Stünitz et al., 2003) or in cases when the recrystallized fraction is higher, display a hybrid between an asymmetric single girdle- and crossed girdle pattern (Fig. 8b; map 2) indicating the slip on prism < a > and rhomb < a > crystal systems (Schmid and Casey, 1986; Law et al., 1990).

SED
7, 1399–1446, 2015

Porphyroclastic remnants of igneous feldspars (Pl_1 and Kfs_1) mainly deform by cataclasis as indicated by clusters of angular, internally fractured and slightly displaced grains (Fig. 5a and c). The relatively small displacement between the individual fragments suggests that fracturing itself plays a minor role in the accommodation of the finite strain. The dominance of Ms_2 at contact sites between porphyroclasts and perpendicular to the shortening direction in contrast to the distribution of more soluble reaction products (Pl_2, Qtz_3, Kfs_2) in strain shadows (Fig. 5e) suggests that mass transfer occurred dominantly by pressure solution at high stress sites and precipitation at low stress sites, involving a fluid phase (Rutter, 1983; Wintsch and Yi, 2002). Accordingly, elements with higher mobility, such as Si^+, Ca^+, Na^+, K^+ were transported by fluid and precipitated in the locally occurring low pressure sites, while the elements of lower mobility, in this case Al^+ were immediately incorporated in the Ms_2 structure which was the new, more stable mineral phase after the dissolution of Kfs_1 and Pl_1. It is important to note that the largest displacement between feldspar fragments occurs where they are surrounded by the thickest mantles of the reaction products (Fig. 5a). This observation indicates strain partitioning from feldspars to these newly created reaction products as soon as a thick enough mantle is formed.

5.3.2 Shear zone centre: phyllonite

Phyllonite A and phyllonite B in the shear zone core structurally display many similarities in terms of Qtz_1 and Qtz_2 microstructures, with intracrystalline plasticity structures in Qtz_1 grains and strong CPO for Qtz_2 grains indicating rotation from porphyroclast orientation towards rhomb < *a* > and prism < *a* > slip systems (Fig. 8b; map 1; Schmid and Casey, 1986) with increasing degree of recrystallization. Minor fraction of the recrystallized quartz (Qtz_2) in the phyllonite A suggests strong strain partitioning into the surrounding muscovite-rich matrix.

The two main differences between the phyllonite A and phyllonite B domains are: (1) quartz-to-muscovite ratio; and (2) matrix-to-clast ratio. Both of which are higher in phyllonite B (Fig. 3a and b; Fig. 6a and b).

SED
7, 1399–1446, 2015

All muscovite in both phyllonites is of metasomatic origin (Ms_2) formed either by a breakdown of igneous biotite or in feldspar reactions (R1 and R2) and distributed by pressure solution processes as Qtz_3 tend to associate with extensional sites in strain shadows and fractures while muscovite concentrate in high stress sites around porphyroclasts, subparallel to the foliation. The consistent SPO of the muscovite grains with elongation subparallel to the shear direction thus may be controlled by syn-tectonic growth in the direction of maximum elongation.

Local variations in muscovite abundance throughout the phyllonites affects the deformation behaviour of quartz. In the fine-grained muscovite-rich layers (Ms_2 = 90–30 %) quartz occurs as Qtz_3-type grains and displays a lack of a clear CPO pattern (Fig. 9b; map 2), where CPO becomes increasing weaker with increasing amount of muscovite (Fig. 9b; map 2i and map 2ii). The lack of CPO coupled with the small grain sizes and phase abundance is consistent with grain boundary sliding (GBS) as the main deformation mechanism (Kruse and Stünitz, 1999; Ree et al., 2005; Svahnberg and Piazolo, 2010). The elongated grain shapes in these domains and the abundance of intracrystalline deformation structures (Fig. 9a and c) suggest that grain boundary sliding was accommodated by dislocation glide (Rybacki et al., 2010; Svahnberg and Piazolo, 2010).

Bulk rock chemistry data suggest that along with the formation of random CPO in these fine-grained muscovite-quartz domains, Si-enrichment occurred (Fig. 10b and c). We suggest that GBS contributed to the generation of a transient porosity by creep cavitation (Závada et al., 2007; Rybacki et al., 2008). In this model, circulation of Si-rich pore fluids in the central parts of the shear zone is facilitated by the creation of dilatant sites by GBS. The resulting low pressure sites attracted pore fluid and facilitated the precipitation and growth of quartz grains in these newly formed intergranular pore spaces (Fusseis et al., 2009). As shown by Menegon et al. (2015) the crystallographic orientation of these precipitated grains is near random, or slightly orientated parallel to the elongation direction.

SED
7, 1399–1446, 2015

In summary, phase mixing in Qtz_3-Ms_2 layers, fine grain sizes and their low relative strength compared to other microstructural domains suggest that continued fluid flow was possible in these areas due to creep cavitation. In the phyllonite B the higher quartz grain sizes, lower muscovite fraction and higher mode of quartz-muscovite mixtures is thus attributed to an advanced stage of grain precipitation from a circulating Si-rich fluid by prolonged operation of creep cavitation processes. Quartz in these muscovite-poor domains then shows the clustering of crystallographic orientations consistent to prism < *a* > and rhomb < *a* > slip systems (Fig. 9b, map 2) indicating that once grain sizes reach sufficiently large sizes, dislocation creep processes become dominant. Consequently, porosity creation by GBS mechanisms is arrested.

A special case of Qtz_3 microstructures can be seen on the tails of larger porphyroclasts (Fig. 9a; map 1) where the CPO shows clustering around the orientation of the adjacent porphyroclast (Fig. 9b; map 1). This is consistent with quartz precipitation from pore fluids at low pressure sites, where the nucleation of the new grains is host-controlled. Their elongated shape subparallel to the main foliation suggests anisotropic growth of minerals commonly reported to occur during pressure-solution processes (Passchier and Trouw, 2005).

Feldspars are rare in the phyllonite and thus play a minor role in the bulk rock rheology. The prominent fracture sets filled by fine-grained muscovite suggest mechano-chemical breakdown processes. The albitic composition of Pl_2 is interpreted as a result of interface-coupled dissolution-precipitation reactions (Putnis, 2009) as indicated by arrested replacement structures in the less altered orthogneiss, where asymmetric albite rims occur around Kfs_1 and Pl_1. Simultaneously, albite grains may also form by neo-nucleation processes from pore fluid where chemically different composition is obtained in response to the disequilibrium state between the deformation conditions/fluid composition and igneous feldspars. This scenario has been previously suggested by (Stünitz and Gerald, 1993) for similar shear zones in Wyangala area. Both of these options indicate fluid-accompanied mass transfer in the shear zone.

SED
7, 1399–1446, 2015

5.4 Deformation conditions

The deformation conditions in the studied shear zone are estimated from: (1) syn-tectonic mineral assemblages, (2) recrystallization microstructures in quartz and (3) CPO patterns in the dynamically recrystallized quartz domains.

The observed reactions (see Sect. 5.2 for details), such as a breakdown of feldspars and biotite to muscovite; albitisation of K-feldspar and plagioclase; and formation of epidote are found to occur in many middle crustal shear zones deformed at green-schist facies conditions (Hippertt, 1998; e.g. Kerrich et al., 1980; Park et al., 2006). In combination with the brittle-ductile rheology expected at middle crustal depths, this gives the first indication on deformation conditions.

More accurate temperature ranges can be obtained from the deformation microstructures in quartz. Undulose extinction, subgrain development, bulged grain boundaries and oriented CPO patterns in the quartz-rich domains indicate the operation of crystal-plastic processes (Hirth and Tullis, 1992; Stipp et al., 2002). Crystal-plasticity in quartz occurs by one of the three mechanisms: bulging (BLG), subgrain rotation (SGR) or high temperature grain boundary migration. Which one of these is the most dominant, largely depends on temperature. In our samples, SGR is the dominant recrystallization regime in quartz. The lobate grain boundaries observed for the recrystallized quartz grains indicate a component of grain boundary migration in BLG recrystallization regime. The transition from BLG to SGR in nature is found to occur at temperatures between 350–400 °C (Stipp et al., 2002), but BLG can also be a result of inter-granular fluids (Mancktelow and Pennacchioni, 2004), imposing uncertainty on the lower temperature constraint.

The conditions at which specific CPO patterns develop, however, do not strongly depend on the absence or presence of fluid (Mancktelow and Pennacchioni, 2004). Our samples show CPO patterns characterized by a combination of basal- and prism- slip (Fig. 8b; corresponding to temperatures between 300 and 400 °C (Schmid and Casey, 1986). Other authors interpret similar patterns as being indicative to deformation at

SED
7, 1399–1446, 2015

temperatures close to 400 °C (Stipp et al., 2002; Lee et al., 2012). This temperature range is supported by the observations of frequent Dauphine twins, which in quartz forms in temperatures between 300 and 400 °C (Wenk et al., 2007; Menegon et al., 2011).

There are no direct indicators for the confining pressure. However, an approximate estimate based on the obtained temperature range (300 to 400 °C) can be drawn using assumption of a normal geothermal gradient (30° km^{-1}) and the average density of continental crust (2.8 $g\,cm^{-3}$) giving depths between 11 and 13 km and pressures between 3.02–3.57 kbar.

5.5 Model for shear zone development

In this section we discuss a conceptual model for the development of the studied brittle-ductile shear zone formed in an initially homogenous granitoid. We describe shear zone development in three temporal stages (Fig. 11). Deformation during stage 2 and 3 is described for the observed two cases, namely case 1: fluid limited and case 2: fluid abundant, seen in the marginal and central domains of the shear zone, respectively.

5.5.1 Stage 1: initiation of the shear zone

We suggest that the first stage of the deformation was marked by high effective stresses and fluid-pressures leading to a brittle failure and formation of a cataclastic fracture zone in the granitic protolith (Fig. 11a). This interpretation is based on the observation of the abundance of the large, only weakly deformed quartz porphyroclasts, in phyllonite A (Fig. 6a). If shear localization had initiated through crystal-plasticity, then quartz would be highly recrystallized as seen in the orthogneiss (Fig. 5a). The preservation of the Qtz_1 grains can only be possible if the weak matrix of reaction products is created early in the shear zone history and strain partitioning occurred before any significant recrystallization of quartz.

SED
7, 1399–1446, 2015

5.5.2 Stage 2: ductile deformation

Stage 2 is marked by ductile deformation in response to the initial cataclastic stage. Brittle failure (Stage 1) resulted in a localized zone utilizing the interconnected fault-fracture mesh precursor as described by Sibson (1996). The increase in permeability and dilatancy-induced pressure fluctuations facilitated the infiltration of external fluids and localized the flow. Subsequent microstructural development and rheology in the shear zone was mainly controlled by its proximity to this initial fracture zone. The sharp boundary separating orthogneiss and phyllonites is interpreted to represents the border between the highly permeable and fractured central domain affected by high fluid fluxes and the low permeability, largely intact crystalline wall rock with a restricted pathways for fluid infiltration (Fig. 11b). This distinction is also reflected in differences in phase distribution (Fig. 3a), microstructures (Fig. 3b, 4, 5) and whole rock chemistry (Fig. 10).

5.5.3 Case 1: deformation at fluid limited conditions

The orthogneiss fabrics at the shear zone margins represent deformation accompanied by a limited fluid influx. Here, the majority of igneous quartz grains behave as a weak phase, developing subgrain- and new grain boundaries through a progressive distortion of the crystal lattice. Only the grains oriented favourable to the basal slip direction are preserved similar to observations from other relatively dry mid-crustal mylonites (Menegon et al., 2011). Up to 70 % of the igneous quartz recrystallized into fine-grained interconnected aggregates, accommodating most of the strain. Simultaneously, the igneous feldspar phenocrysts underwent fragmentation by brittle failure (Fig. 5).

Syn-tectonic retrograde reactions of igneous biotite (Bt_1) and muscovite (Ms_1) released pore fluid, which migrated along the fractures and grain boundaries facilitating microcrack-formation, pressure-solution processes, and mineral reactions to weak fine-grained polycrystalline phases (Fig. 5). However the low amount of fluid available from the local reservoirs, and possibly the slow rates of its release do not permit rapid weak-

SED
7, 1399–1446, 2015

ening to take place. Consequently, strain localization is limited and deformation occurs throughout the rock.

5.5.4 Case 2: deformation at fluid abundant conditions

In the following, we assume that fabrics in phyllonite A represent an early stage in the evolution of the central domains. This assumption is based on the fact that mineralogically and chemically phyllonite A is closer to the wall rock composition than to phyllonite B (Fig. 10).

In the shear zone centre, the cataclastic protolith provides easy pathways and creates dilatational low pressure sites attracting external fluids, leading to widespread and rapid mineral reactions of the metastable igneous assemblage. As a result, the load-bearing feldspar framework is rapidly destroyed and the newly produced matrix of fine-grained reaction products localizes the strain and arrests any further deformation in the quartz porphyroclasts (Qtz_1). Consequently, quartz porphyroclasts preserve sizes similar to the igneous grains in the wall rock as it is only weakly recrystallized (Fig. 6a). The deformation is controlled by the weak fine-grained matrix through a combination of pressure solution and GBS/cavitation creep processes. Due to the low activation energy required, these mechanisms can lead to significant shape- and volume changes of minerals even at low differentials stresses (Wintsch and Yi, 2002).

5.5.5 Stage 3: continued fluid percolation leading to phase mixing and volume increase by cavitation creep

Phyllonite B represents a phyllonite A fabric, which is modified by a prolonged fluid percolation (Fig. 11c). The chemical and mineral evidence of SiO_2 gains indicates that significant amount of quartz in phyllonite B is incorporated during this alteration. We suggest that this "new" quartz have been added in phyllonite B by a precipitation from a pore-fluid in transient dilatational sites, similar to the creep cavitation process described by Fusseis et al. (2009) and Menegon et al. (2015). The creation of cavities

SED
7, 1399–1446, 2015

occurs in muscovite-rich layers and sites of high rheological contrasts, such as pressure shadows, where dilation is higher due to the fabric anisotropy. The resultant drop in pore-fluid pressure draws in fluid leading to a precipitation of the quartz nucleus. Further, the size of these "new" grains is increased by continuous precipitation of quartz. This process continues until the increasing grain sizes and quartz mode in initially muscovite-rich layers lead to the switch to dislocation creep mechanisms. The resulting drop in strain rates by switching from GBS-deformation to dislocation creep, arrests or greatly decreases the porosity generation and creep cavitation processes, leading to a rheological hardening. The resulting microstructure displays CPO and resembles Qtz_2 grains, which are originally formed by dynamic recrystallization. This interpretation is supported by the fact that the "reaction" quartz (Qtz_3) can not account for all the increase in quartz mode in phyllonite B compared to the wall rock (Fig. 3b), and thus at least part of the Qtz_2 microstructure must also have an external origin.

We suggest that the shear zone may be abandoned completely once it becomes rheologically hard. This could happen when the rock deforms dominantly by dislocation creep and not cavitation creep due to fluid flux and cavitation creep-related increase in quartz grain size and abundance.

6 Conclusions

The studied shear zone represents an example of a brittle-ductile deformation in middle crust accompanied by circulating syn-deformational fluids. The fluid flow was highly localized in narrow central parts of the shear zone due to a cataclastic precursor and rapid metasomatic reactions, which created necessary porosity for fluid infiltration. As a result two structurally and chemically different domains developed across the shear zone, depending on the availability of the fluid. The "fluid-limited" shear zone margins experienced little impact of chemical processes on the deformation, preserving the granitic assemblages similar to the wall rock and deforming mainly by crystal-plastic processes in quartz. In contrast, the "wet" shear zone centre experienced extreme

SED
7, 1399–1446, 2015

chemical alteration, rapid reduction in grain sizes by chemical break down reactions and a development of interconnected foliation partitioning the strain. The fine grain sizes further enabled fluid infiltration and creep cavitation coupled with grain boundary sliding in the highly anisotropic reaction fabric. As a result circulating pore fluids lead to further alteration of the shear zone fabric and rheology by mineral reactions and mass transfer. The dynamic system enabled the transportation of large amount of metasomatic fluid leading to a significant mass increase by ~ 250 %.

In summary, the existence of an initial brittle fracture system facilitated enhanced fluid flow, rapid reaction and subsequent phase mixing. This then enabled strain localization and focussed fluid flow due to creep cavitation and associated fluid pumping.

Acknowledgements. Financial support through Discovery Project (DP120102060) to S. Piazolo and internal funding to L. Spruzeniece (Department of Earth and Planetary Sciences, Macquarie University) is hereby acknowledged. This study used instrumentation funded by ARC LIEF and DEST Systemic Infrastructure Grants, Macquarie University and Industry.

We thank David Adams for his help with SEM-based analyses as well as to Paul Lennox and Karol Czarnota for providing a copy of their unpublished work on Wyangala area regional geology. Special thanks to Paul Lennox for the introduction to the field. This is contribution XXX from the ARC Centre of Excellence for Core to Crust Fluid Systems (www.ccfs.mq.edu.au) and XXX from the GEMOC Key Centre (www.gemoc.mq.edu.au).

References

Bestmann, M. and Prior, D. J.: Intragranular dynamic recrystallization in naturally deformed calcite marble: diffusion accommodated grain boundary sliding as a result of subgrain rotation recrystallization, J. Struct. Geol., 25, 1597–1613, doi:10.1016/S0191-8141(03)00006-3, 2003.

Billia, M. A., Timms, N. E., Toy, V. G., Hart, R. D., and Prior, D. J.: Grain boundary dissolution porosity in quartzofeldspathic ultramylonites: implications for permeability enhancement and weakening of mid-crustal shear zones, J. Struct. Geol., 53, 2–14, doi:10.1016/j.jsg.2013.05.004, 2013.

SED
7, 1399–1446, 2015

Bos, B. and Spiers, C. J.: Frictional-viscous flow of phyllosilicate-bearing fault rock: microphysical model and implications for crustal strength profiles, J. Geophys. Res., 107, 2028, doi:10.1029/2001JB000301, 2002.
Brander, L., Svahnberg, H., and Piazolo, S.: Brittle-plastic deformation in initially dry rocks at fluid-present conditions: transient behaviour of feldspar at mid-crustal levels, Contrib. Mineral. Petr., 163, 403–425, doi:10.1007/s00410-011-0677-5, 2012.
Byerlee, J.: Friction, overpressure and fault normal compression, Geophys. Res. Lett., 17, 2109, doi:10.1029/GL017i012p02109, 1990.
Czarnota, K.: The Geology and Structure in the Wyangala Dam Area of the Lachlan Fold Belt, NSW, University of New South Wales, 2002.
Eilu, P., Mikucki, E. J., and Dugdale, A. L.: Alteration zoning and primary geochemical dispersion at the Bronzewing lode-gold deposits, Western Australia, Miner. Depos., 36, 13–31, doi:10.1007/s001260050283, 2001.
Foster, D. a., Gray, D. R., Spaggiari, C., Kamenov, G., and Bierlein, F. P.: Palaeozoic Lachlan orogen, Australia; accretion and construction of continental crust in a marginal ocean setting: isotopic evidence from Cambrian metavolcanic rocks, Geol. Soc. Spec. Publ., 318, 329–349, doi:10.1144/SP318.12, 2009.
Fusseis, F. and Handy, M. R.: Micromechanisms of shear zone propagation at the brittle-viscous transition, J. Struct. Geol., 30, 1242–1253, doi:10.1016/j.jsg.2008.06.005, 2008.
Fusseis, F., Liu, J., Hough, R. M., and Carlo, F. De: Creep cavitation can establish a dynamic granular fluid pump in ductile shear zones, Nature, 459, 974–977, doi:10.1038/nature08051, 2009.
Glen, R.: Thrust, extensional and strike-slip tectonics in an evolving Palaeozoic orogen – a structural synthesis of the Lachlan Orogen of southeastern Australia, Tectonophysics, 214, 341–380, doi:10.1016/0040-1951(92)90205-K, 1992.
Goncalves, P., Oliot, E., Marquer, D., and Connolly, J. A. D.: Role of chemical processes on shear zone formation: an example from the grimsel metagranodiorite (Aar massif, Central Alps), J. Metamorph. Geol., 30, 703–722, doi:10.1111/j.1525-1314.2012.00991.x, 2012.
Grant, J. A.: The isocon diagram-a simple solution to Gresens' equation for metasomatic alteration., Econ. Geol., 81, 1976–1982, doi:10.2113/gsecongeo.81.8.1976, 1986.
Gray, D. R.: Tectonics of the southeastern Australian Lachlan Fold Belt: structural and thermal aspects, Geol. Soc. Spec. Publ., 121, 149–177, doi:10.1144/GS.L.S~P.1997.121.01.07, 1997.

SED
7, 1399–1446, 2015

Gresens, R. L.: Composition–volume relationships of metasomatism, Chem. Geol., 2, 47–65, doi:10.1016/0009-2541(67)90004-6, 1967.
Handy, M., Hirth, G., and Burgmann, R.: Continental fault structure and rheology from the frictional-to-viscous transition downward, in: Continental Fault Structure and Rheology from the Frictional-to-Viscous Transition Downward, 139–181, 2007.
Hippertt, J. F.: Breakdown of feldspar, volume gain and lateral mass transfer during mylonitization of granitoid in a low metamorphic grade shear zone, J. Struct. Geol., 20, 175–193, doi:10.1016/S0191-8141(97)00083-7, 1998.
Hirth, G. and Tullis, J.: Dislocation creep regimes in quartz aggregates, J. Struct. Geol., 14, 145–159, doi:10.1016/0191-8141(92)90053-Y, 1992.
Karato, S.-I., Paterson, M. S., and FitzGerald, J. D.: Rheology of synthetic olivine aggregates: influence of grain size and water, J. Geophys. Res., 91, 8151, doi:10.1029/JB091iB08p08151, 1986.
Kerrich, R., Allison, I., Barnett, R. L., Moss, S., and Starkey, J.: Microstructural and chemical transformations accompanying deformation of granite in a shear zone at Mifiville, Switzerland; with implications for stress corrosion cracking and superplastic flow, Contrib. Mineral. Petr., 73, 221–242, doi:10.1007/BF00381442, 1980.
Kilian, R., Heilbronner, R., and Stünitz, H.: Quartz grain size reduction in a granitoid rock and the transition from dislocation to diffusion creep, J. Struct. Geol., 33, 1265–1284, doi:10.1016/j.jsg.2011.05.004, 2011.
Kohlstedt, D. L., Evans, B., and Mackwell, S. J.: Strength of the lithosphere: constraints imposed by laboratory experiments, J. Geophys. Res., 100, 17587, doi:10.1029/95JB01460, 1995.
Kolb, J., Rogers, A., Meyer, F. M., and Vennemann, T. W.: Development of fluid conduits in the auriferous shear zones of the Hutti Gold Mine, India: evidence for spatially and temporally heterogeneous fluid flow, Tectonophysics, 378, 65–84, doi:10.1016/j.tecto.2003.10.009, 2004.
Kretz, R.: Symbols for rock-forming minerals, Am. Mineral., 68, 277–279, 1983.
Kruse, R. and Stünitz, H.: Deformation mechanisms and phase distribution in mafic high-temperature mylonites from the Jotun Nappe, southern Norway, Tectonophysics, 303, 223–249, doi:10.1016/S0040-1951(98)00255-8, 1999.
Kruse, R., Stünitz, H., and Kunze, K.: Dynamic recrystallization processes in plagioclase porphyroclasts, J. Struct. Geol., 23, 1781–1802, doi:10.1016/S0191-8141(01)00030-X, 2001.

SED
7, 1399–1446, 2015

Law, R. D., Schmid, S. M., and Wheeler, J.: Simple shear deformation and quartz crystallographic fabrics: a possible natural example from the Torridon area of NW Scotland, J. Struct. Geol., 12, 29–45, doi:10.1016/0191-8141(90)90046-2, 1990.
Lee, P. E., Jessup, M. J., Shaw, C. A., Hicks, G. L., and Allen, J. L.: Strain partitioning in the mid-crust of a transpressional shear zone system: insights from the Homestake and Slide Lake shear zones, central Colorado, J. Struct. Geol., 39, 237–252, doi:10.1016/j.jsg.2012.02.006, 2012.
Lennox, P., Trzebski, R., Armstrong, R., and Siebel, W.: Structural evolution and granite chronology of the central Molong Zone, Eastern Lachlan Fold Belt, Australia, Aust. J. Earth Sci., 52, 79–99, doi:10.1080/08120090500109102, 2005.
Lennox, P. G., Forster, M. a., and Williams, I. S.: Emplacement and deformation ages of the Wyangala Granite, Cowra, NSW, Aust. J. Earth Sci., 61, 607–618, doi:10.1080/08120099.2014.897648, 2014.
Mancktelow, N. S.: How ductile are ductile shear zones?, Geology, 34, 345–348, doi:10.1130/G22260.1, 2006.
Mancktelow, N. S. and Pennacchioni, G.: The influence of grain boundary fluids on the microstructure of quartz-feldspar mylonites, J. Struct. Geol., 26, 47–69, doi:10.1016/S0191-8141(03)00081-6, 2004.
Mariani, E., Brodie, K. H., and Rutter, E. H.: Experimental deformation of muscovite shear zones at high temperatures under hydrothermal conditions and the strength of phyllosilicate-bearing faults in nature, J. Struct. Geol., 28, 1569–1587, doi:10.1016/j.jsg.2006.06.009, 2006.
Marsh, J. H., Johnson, S. E., Yates, M. G., and West, D. P.: Coupling of deformation and reactions during mid-crustal shear zone development: an in situ frictional-viscous transition, J. Metamorph. Geol., 27, 531–553, doi:10.1111/j.1525-1314.2009.00841.x, 2009.
Menegon, L. and Pennacchioni, G.: Local shear zone pattern and bulk deformation in the Gran Paradiso metagranite (NW Italian Alps), Int. J. Earth Sci., 99, 1805–1825, doi:10.1007/s00531-009-0485-6, 2010.
Menegon, L., Pennacchioni, G., and Spiess, R.: Dissolution-precipitation creep of K-feldspar in mid-crustal granite mylonites, J. Struct. Geol., 30, 565–579, doi:10.1016/j.jsg.2008.02.001, 2008.
Menegon, L., Piazolo, S., and Pennacchioni, G.: The effect of Dauphin twinning on plastic strain in quartz, Contrib. Mineral. Petr., 161, 635–652, doi:10.1007/s00410-010-0554-7, 2011.

SED
7, 1399–1446, 2015

Menegon, L., Fusseis, F., Stünitz, H., and Xiao, X.: Creep cavitation bands control porosity and fluid flow in lower crustal shear zones, Geol., 43, 227–230, doi:10.1130/G36307.1, 2015.
Oliot, E., Goncalves, P., Schulmann, K., Marquer, D., and Lexa, O.: Mid-crustal shear zone formation in granitic rocks: constraints from quantitative textural and crystallographic preferred orientations analyses, Tectonophysics, 612–613, 63–80, doi:10.1016/j.tecto.2013.11.032, 2014.
Park, Y., Yoo, S. H., and Ree, J. H.: Weakening of deforming granitic rocks with layer development at middle crust, J. Struct. Geol., 28, 919–928, doi:10.1016/j.jsg.2006.02.005, 2006.
Passchier, C. and Trouw, R.: Microtectonics, 2005.
Paterson, S. R. and Tobisch, O. T.: Rates of processes in magmatic arcs: implications for the timing and nature of pluton emplacement and wall rock deformation, J. Struct. Geol., 14, 291–300, doi:10.1016/0191-8141(92)90087-D, 1992.
Paterson, S. R., Tobisch, O. T., and Morand, V. J.: The influence of large ductile shear zones on the emplacement and deformation of the Wyangala Batholith, SE Australia, J. Struct. Geol., 12, 639–650, doi:10.1016/0191-8141(90)90079-E, 1990.
Poirier, J. P.: Shear localization and shear instability in materials in the ductile field, J. Struct. Geol., 2, 135–142, doi:10.1016/0191-8141(80)90043-7, 1980.
Prior, D. J., Wheeler, J., Peruzzo, L., Spiess, R., and Storey, C.: Some garnet microstructures: an illustration of the potential of orientation maps and misorientation analysis in microstructural studies, J. Struct. Geol., 24, 999–1011, doi:10.1016/S0191-8141(01)00087-6, 2002.
Putnis, A.: Mineral Replacement Reactions, Rev. Mineral. Geochem., 70, 87–124, doi:10.2138/rmg.2009.70.3, 2009.
Ree, J. H., Kim, H. S., Han, R., and Jung, H.: Grain-size reduction of feldspars by fracturing and neocrystallization in a low-grade granitic mylonite and its rheological effect, Tectonophysics, 407, 227–237, doi:10.1016/j.tecto.2005.07.010, 2005.
Rolland, Y., Cox, S., Boullier, A. M., Pennacchioni, G., and Mancktelow, N.: Rare earth and trace element mobility in mid-crustal shear zones: insights from the Mont Blanc Massif (Western Alps), Earth Planet. Sc. Lett., 214, 203–219, doi:10.1016/S0012-821X(03)00372-8, 2003.
Rutter, E. H.: Pressure solution in nature, theory and experiment, J. Geol. Soc. London, 140, 725–740, doi:10.1144/gsjgs.140.5.0725, 1983.
Rybacki, E., Wirth, R., and Dresen, G.: High-strain creep of feldspar rocks: implications for cavitation and ductile failure in the lower crust, Geophys. Res. Lett., 35, 1–5, doi:10.1029/2007GL032478, 2008.

SED
7, 1399–1446, 2015

Rybacki, E., Wirth, R., and Dresen, G.: Superplasticity and ductile fracture of synthetic feldspar deformed to large strain, J. Geophys. Res.- Sol. Ea., 115, 1–14, doi:10.1029/2009JB007203, 2010.
Schmid, S. M. and Casey, M.: Complete fabric analysis of some commonly observed quartz *c* axis fabrics, Miner. Rock Deform. Lab. Stud., 36, 263–286, 1986.
Scholz, C. H.: Fault mechanics, in: Treatise on Geophysics, vol. 6, 441–483., 2007.
Sibson, R. H.: Fault zone model, heat flow, and the depth distribution of earthquakes in the continental crust of the United States, B. Seismol. Soc. Am., 72, 151–163, 1982.
Sibson, R. H.: Structural permeability of fluid-driven fault-fracture meshes, J. Struct. Geol., 18, 1031–1042, doi:10.1016/0191-8141(96)00032-6, 1996.
Squire, R. J. and Crawford, A. J.: Magmatic characteristics and geochronology of Ordovician igneous rocks from the Cadia-Neville region, New South Wales: implications for tectonic evolution, Aust. J. Earth Sci., 54, 293–314, doi:10.1080/08120090601147001, 2007.
Stipp, M., Stünitz, H., Heilbronner, R., and Schmid, S. M.: The eastern Tonale fault zone: a "natural laboratory" for crystal plastic deformation of quartz over a temperature range from 250 to 700 °C, J. Struct. Geol., 24, 1861–1884, doi:10.1016/S0191-8141(02)00035-4, 2002.
Stünitz, H. and Gerald, J. D. F.: Deformation of granitoids at low metamorphic grade. II: Granular flow in albite-rich mylonites, Tectonophysics, 221, 299–324, doi:10.1016/0040-1951(93)90164-F, 1993.
Stünitz, H., Fitz Gerald, J., and Tullis, J.: Dislocation generation, slip systems, and dynamic recrystallization in experimentally deformed plagioclase single crystals, Tectonophysics, 372, 215–233, doi:10.1016/S0040-1951(03)00241-5, 2003.
Svahnberg, H. and Piazolo, S.: The initiation of strain localisation in plagioclase-rich rocks: insights from detailed microstructural analyses, J. Struct. Geol., 32, 1404–1416, doi:10.1016/j.jsg.2010.06.011, 2010.
Tullis, J. and Yund, R. A.: Hydrolytic weakening of experimentally deformed Westerly granite and Hale albite rock, J. Struct. Geol., 2, 439–451, doi:10.1016/0191-8141(80)90005-X, 1980.
Urai, J. L., Spiers, C. J., Zwart, H. J., and Lister, G. S.: Weakening of rock salt by water during long-term creep, Nature, 324, 554–557, doi:10.1038/324554a0, 1986.
Vandenberg, A. H. and Stewart, I.: Ordovician terranes of the southeastern Lachlan Fold Belt: stratigraphy, structure and palaeogeographic reconstruction, Tectonophysics, 214, 159–176, doi:10.1016/0040-1951(92)90195-C, 1992.

SED
7, 1399–1446, 2015

Wenk, H.-R., Bortolotti, M., Barton, N., Oliver, E., and Brown, D.: Dauphiné twinning and texture memory in polycrystalline quartz, Phys. Chem. Miner., 34, 599–607, doi:10.1007/s00269-007-0174-6, 2007.

White, S.: Geological significance of recovery and recrystallization processes in quartz, Tectonophysics, 39, 143–170, 1977.

White, S. H. and Knipe, R. J.: Transformation- and reaction-enhanced ductility in rocks, J. Geol. Soc. London, 135, 513–516, doi:10.1144/gsjgs.135.5.0513, 1978.

Wintsch, R. P. and Yeh, M. W.: Oscillating brittle and viscous behavior through the earthquake cycle in the Red River Shear Zone: monitoring flips between reaction and textural softening and hardening, Tectonophysics, 587, 46–62, doi:10.1016/j.tecto.2012.09.019, 2013.

Wintsch, R. P. and Yi, K.: Dissolution and replacement creep: a significant deformation mechanism in mid-crustal rocks, J. Struct. Geol., 24, 1179–1193, doi:10.1016/S0191-8141(01)00100-6, 2002.

Závada, P., Schulmann, K., Konopásek, J., Ulrich, S., and Lexa, O.: Extreme ductility of feldspar aggregates - Melt-enhanced grain boundary sliding and creep failure: rheological implications for felsic lower crust, J. Geophys. Res. Sol. Ea., 112, doi:10.1029/2006JB004820, 2007.

SED
7, 1399–1446, 2015

Table 1. Whole rock geochemical data. Major element concentrations and mass balance calculations of the selected samples from wall rock, orthogneiss, phyllonite A and phyllonite B. Detection error for the measurements is given in Table A1.

	Measured concentrations (wt. %)				Scaling factor	As plotted in isocon diagrams (wt. %)				Mass change rel. to Al_2O_3 (Eq. 1) (%)		
Sample Location	W17 wall	W13b orthogneiss	W21b phyllonite A	W21c phyllonite B		W17 wall	W13b orthogneiss	W21b phyllonite A	W21c phyllonite B	W13b orthogneiss	W21b phyllonite A	W21c phyllonite B
Na_2O	2.51	2.47	0.48	0.04	25	62.80	61.85	12.03	1.03	−1.62	−78.51	−94.46
MgO	0.89	0.80	0.66	0.26	35	31.15	28.11	23.00	9.10	−9.87	−17.14	−0.89
Al_2O_3	13.04	13.05	11.62	3.84	5	65.19	65.26	58.08	19.22	0.00	0.00	0.00
SiO_2	72.89	72.13	77.94	92.75	1	36.45	36.07	38.97	46.37	−1.15	20.01	331.66
P_2O_5	0.13	0.12	0.03	0.01	60	7.80	7.20	1.56	0.84	−7.79	−77.55	−63.46
K_2O	4.39	4.11	3.30	1.14	9	39.55	37.03	29.74	10.27	−6.47	−15.60	−11.90
CaO	1.73	1.89	1.21	0.60	25	43.23	47.20	30.23	14.90	9.08	−21.52	16.95
TiO_2	0.41	0.41	0.25	0.07	50	20.40	20.65	12.35	3.55	1.12	−32.05	−40.96
Mn_3O_4*	0.05	0.04	0.03	0.01	50	2.50	1.95	1.30	0.65	−22.08	−41.63	−11.79
Fe_2O_3	2.67	2.72	2.56	1.09	20	53.38	54.40	51.24	21.86	1.80	7.74	38.94
Sum	98.71	97.75	98.07	99.82						−1.08	11.50	243.06
LOI (calc)	1.29	2.25	1.94	0.18						74.40	68.76	−51.76
LOI (meas)	0.95	1.18	2.13	0.63						24.08	151.66	124.99
Total	99.66	98.93	100.20	100.45						−0.84	12.84	241.94
							Total mass change (Eq. 2)			−0.11	12.24	239.27

SED
7, 1399–1446, 2015

Table A1. Absolute and relative detection error for the whole rock chemical data.

Major element (wt. %)	Absolute error (wt. %)	Relative error (%)
90	±0.1 to 0.2	±0.1 to 0.2
50	±0.1	±0.2
10	±0.05 to 0.1	±0.5 to 1
1	±0.01 to 0.02	±1 to 2

SED
7, 1399–1446, 2015

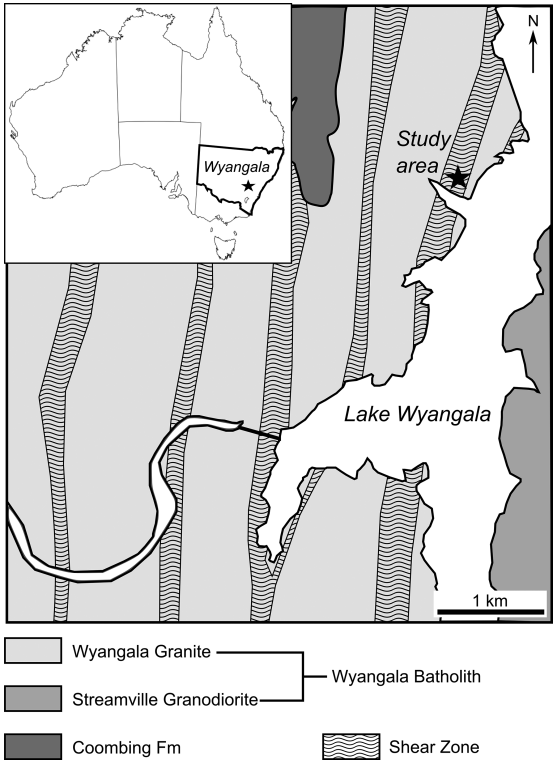

Figure 1. Locality map showing the position of Wyangala area in a regional context (inset) and the location of the studied outcrop on a simplified geological map (modified after Czarnota, 2002).

SED
7, 1399–1446, 2015

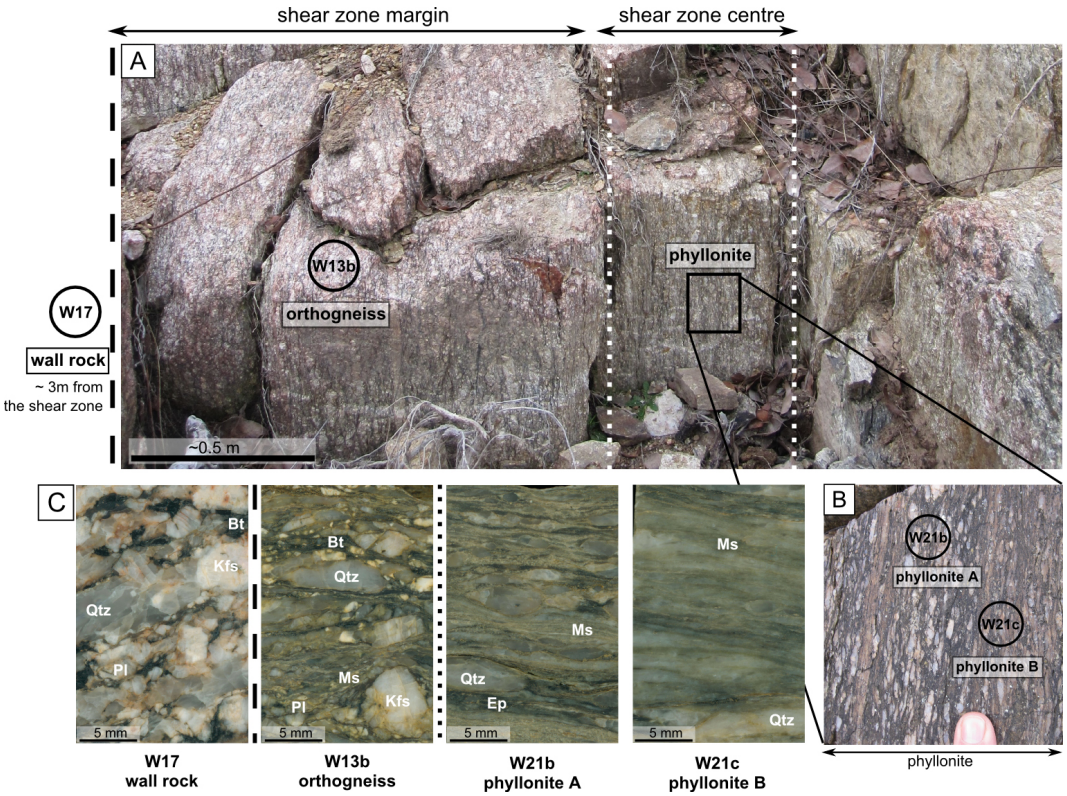

Figure 2. Outcrop and hand specimens. **(a)** Photo of the studied outcrop showing the different shear zone domains and collection sites of 4 studied representative samples (W17; W13b; W21b; W21c), which were further used for all the quantitative analysis; **(b)** fine-scale alternation between the phyllonite A and phyllonite B in the central part of the shear zone; **(c)** sequence of representative samples collected in a transect across the shear zone.

SED
7, 1399–1446, 2015

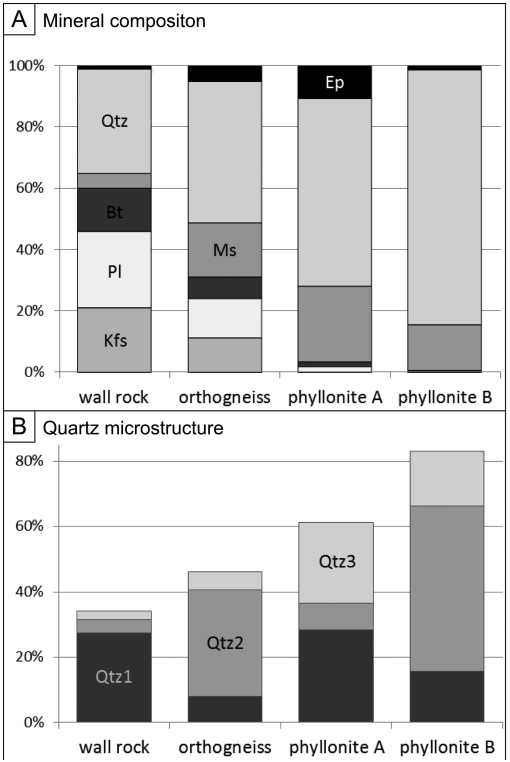

Figure 3. (a) Measured modal mineral compositions of each shear zone domain (Kfs – K-feldspar, Pl – plagioclase, Bt – biotite, Ms – muscovite, Qtz – quartz, Ep – epidote); **(b)** the estimated modal amounts of different quartz microstructures in each shear zone domain (see text for details).

SED
7, 1399–1446, 2015

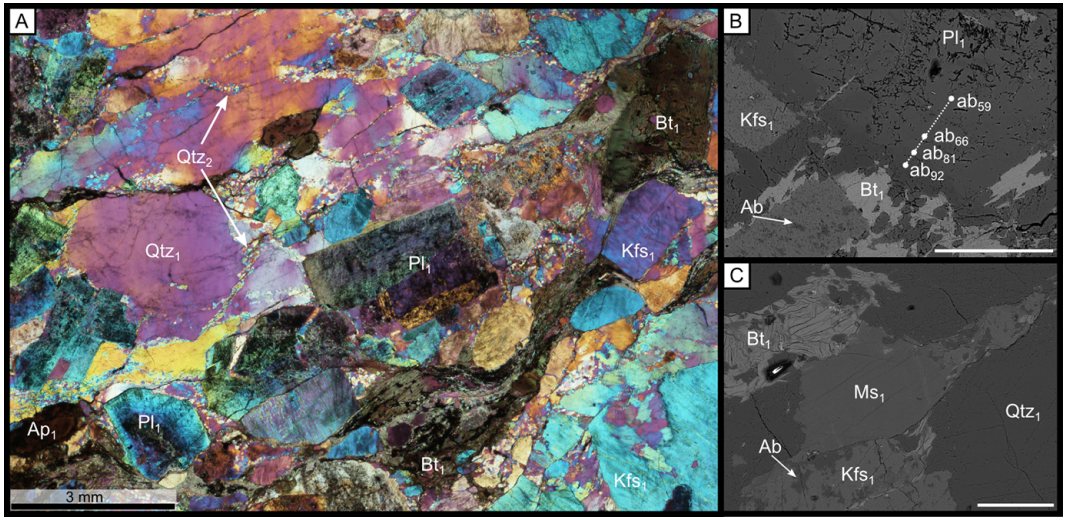

Figure 4. Typical microstructures and mineral assemblages in the wall rock, scale bar for **(b)**–**(c)** is 200 µm. **(a)** Optical micrograph (crossed polarizers with gypsum plate inserted) showing undulose extinction in quartz (Qtz_1), euhedral feldspar grains (Pl_1, Kfs_1), and Bt_1. Arrows points to developing Qtz_2 domains, which often associate with Qtz_1 grains; **(b)** BSE image showing compositional zonation in plagioclase Pl_1 and albite exsolution lamellae in Kfs_1; **(c)** BSE image showing the microstructure of the igneous phyllosilicates (Bt_1 and Ms_1) characterized by large cleaved and kinked grains.

SED
7, 1399–1446, 2015

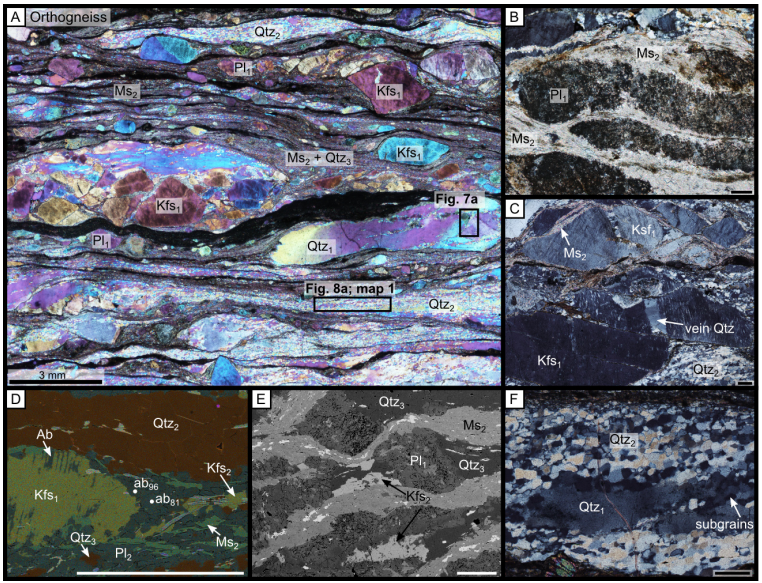

Figure 5. Typical microstructures and mineralogy in orthogneiss, scale bar for **(b)**–**(f)** is 200 µm. **(a)** An overview optical micrograph (crossed polarizers with gypsum plate inserted) showing large fractured feldspar grains (Kfs_1 and Pl_1), undulose extinction in quartz (Qtz_1), fine-grained, monomineralic domains of Qtz_2 and thin, muscovite-rich mantles surrounding Kfs_1 and Pl_1; **(b)** optical micrograph (crossed polarizers) showing fine-grained muscovite (Ms_2) corona around plagioclase (Pl_1); **(c)** optical micrograph (crossed polarizers) showing book-shelf fractures in K-feldspar (Kfs_1) and muscovite (Ms_2) aggregates associating with fractures and grain boundaries; **(d)** EDX-derived compositional map showing Kfs_1 grain with albite exsolution lamellae and Pl_2, Qtz_3, Kfs_2 and Ms_2 in the strain shadow, where the small plagioclase grains have variable compositions typically having oligoclase cores and albite rims; **(e)** BSE image showing Pl_1 porphyroclasts with Qtz_3 and Kfs_2 in the strain shadows and Ms_2 forming strain caps; **(f)** optical micrograph (crossed polarizers) showing Qtz_1 grain surrounded by Qtz_2 aggregates. Qtz_1 displays undulose extinction and subgrains exhibiting similar sizes to Qtz_2 grains.

SED
7, 1399–1446, 2015

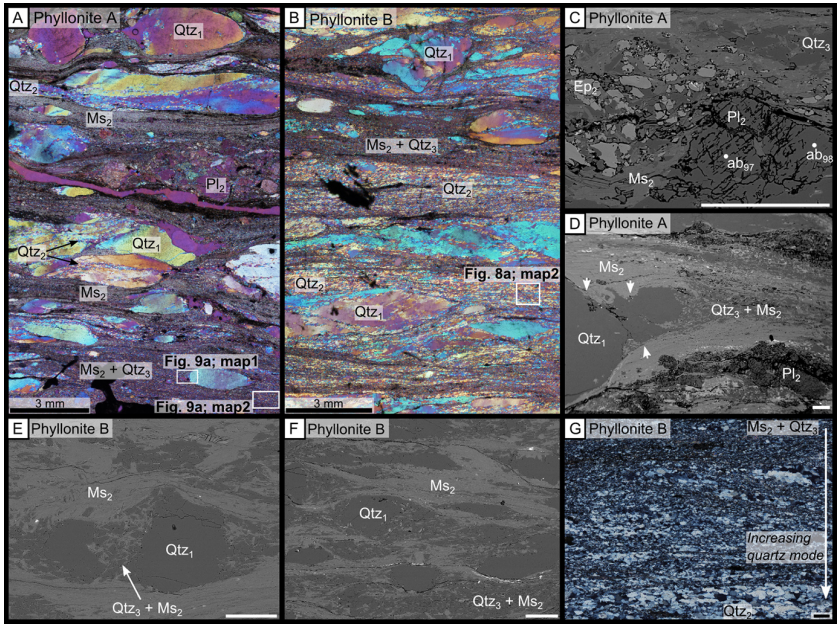

Figure 6. Typical microstructures and mineralogy in phyllonite A and B, scale bar for **(b)**–**(g)** is 200 µm. **(a)**–**(b)** Optical micrographs (crossed polarizers with gypsum plate inserted), **(c)**–**(f)** BSE images and **(g)** optical micrograph with crossed polarizers; **(a)** overview of microstructures in phyllonite A; **(b)** overview of microstructures in phyllonite B; **(c)** fractured grain of albitic plagioclase (Pl_2) surrounded by mantle of muscovite, epidote and quartz; **(d)** quartz grain having irregular boundaries with muscovite (noted with arrows) and mixed quartz-muscovite layer in the strain shadow; **(e)** the extensional site between two Qtz_1 grains filled with mixed quartz-muscovite aggregates; **(f)** Qtz_1 grains in muscovite-quartz matrix, showing the tendency of monomineralic muscovite layers to occur parallel to the shear direction and quartz-muscovite mixtures to occur in the strain shadows. **(g)** Fine-grained matrix in phyllonite B showing variations of quartz and muscovite modal amounts on a millimetre scale.

SED
7, 1399–1446, 2015

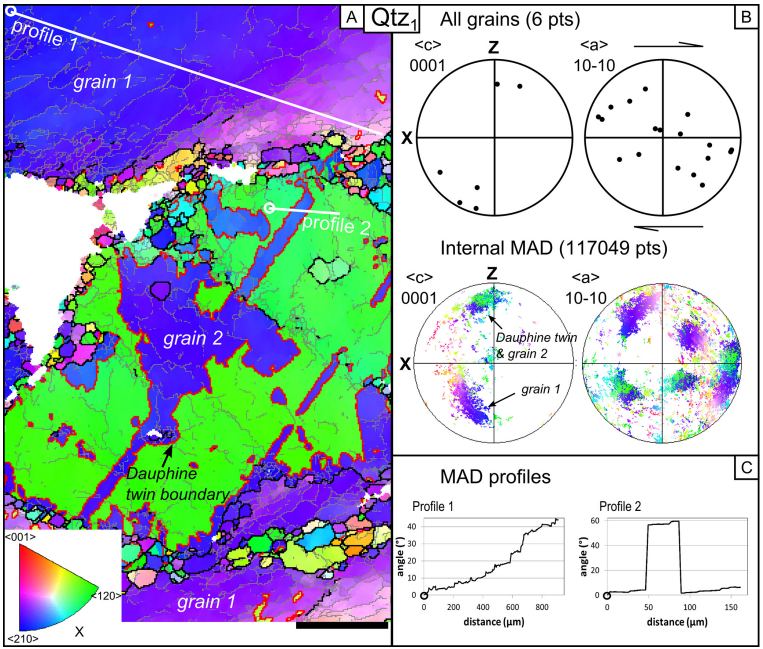

Figure 7. (a) GB (grain boundary) + IPF (inverse pole figure) map of a Qtz_1 grain from orthogneiss (acquisition location marked in Fig. 5a), scale bar is 200 µm. Subgrain boundaries are marked as grey lines, grain boundaries are black and Dauphine twin boundaries are red. White pixels are non-indexed points or other phases. **(b)** Pole figure plots showing the crystallographic orientations of all analysed Qtz_1 grains (top) and internal misorientation angle distributions of each pixel in the map **(a)** (bottom). **(c)** Misorientation profiles across two selected regions in the map **(a)**, where the profiles are marked with white lines and the white circle represents starting position.

SED
7, 1399–1446, 2015

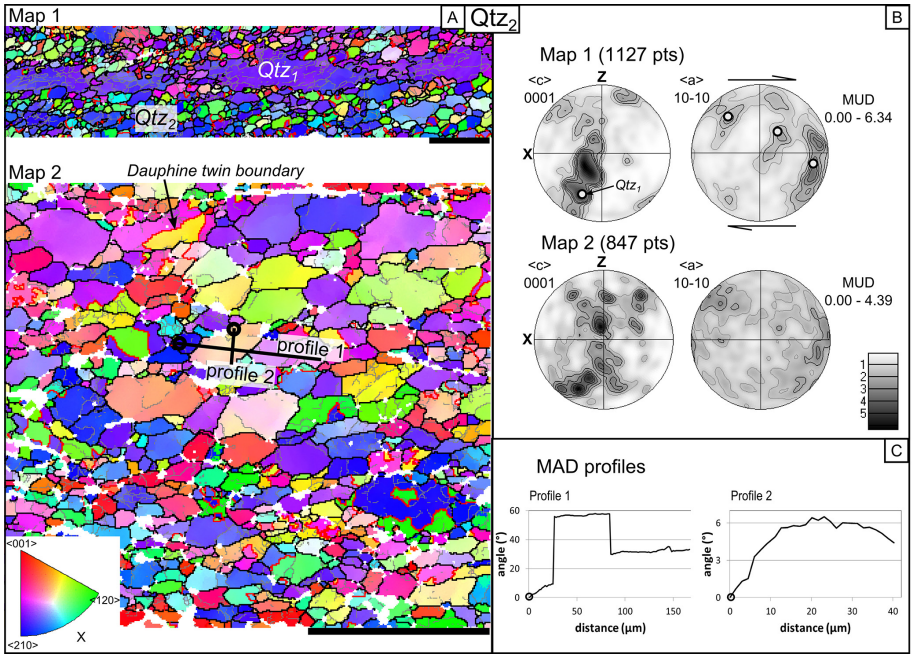

Figure 8. (a) GB (grain boundary) + IPF (inverse pole figure) map of Qtz_2 microstructures (acquisition locations marked in Figs. 5a and 6b), scale bars 200 µm. **(b)** Pole figures of the crystallographic orientation data for map 1 and map 2, plotted as one point per grain using equal area projection and the upper hemisphere. The white dot in the pole figure for map 1 marks the orientation of the Qtz_1 grain, which occurs at the central part of the Qtz_2 domain. **(c)** Misorientation profiles across two selected regions in the map 2, where the profiles are marked by black lines and the circle represents starting position.

SED
7, 1399–1446, 2015

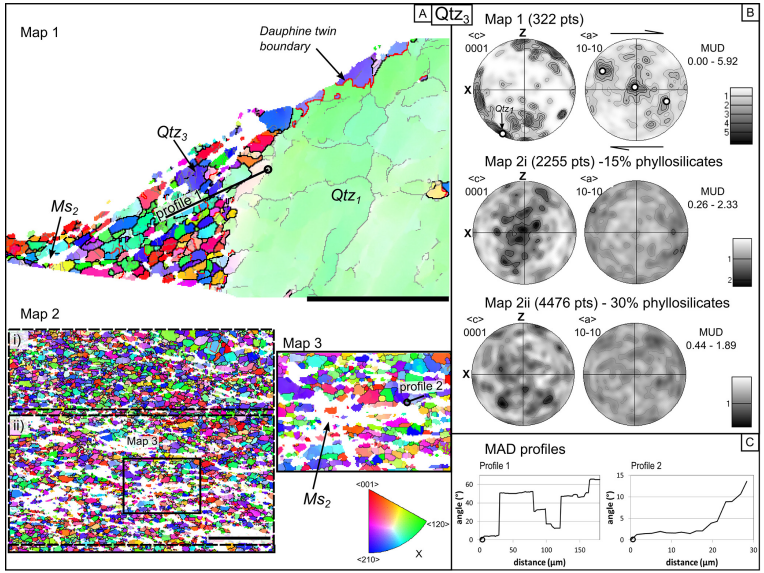

Figure 9. (a) GB (grain boundary) + IPF (inverse pole figure) map of Qtz_3 microstructures in phyllonites (acquisition locations marked in Fig. 6a). Map 2 is separated in two areas for pole figure plots. Area i represents quartz rich part (15 % muscovite), while area ii has large muscovite mode (30 % muscovite). Map 3 is an enlarged image from map 2ii, showing subgrain scale microstructures, scale bars are 200 µm. **(b)** Pole figures of the crystallographic orientation data for map 2i and map 2ii, plotted as one point per grain using equal area projection and the upper hemisphere. The white dot in the pole figure for map 1 marks the orientation of the Qtz_1 grain, which occurs at the central part of Qtz_2 domain. **(c)** Misorientation profiles across two selected regions in map 1 and map 3, where the profiles are marked by black lines and the circle represents starting position.

SED
7, 1399–1446, 2015

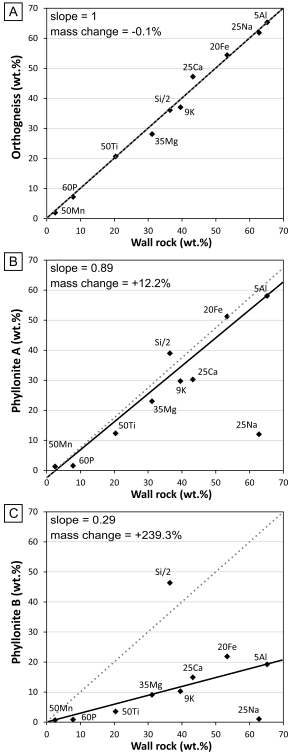

Figure 10. Isocon diagrams (Grant, 1986) showing major element concentrations for: **(a)** orthogneiss, **(b)** phyllonite A, **(c)** phyllonite B plotted against the wall rock composition. The dashed line represents a situation of a zero mass change. The isocon (solid line) is constructed assuming immobile Al_2O_3. Elements enriched in the altered domains lie above the isocon, the elements, which are depleted lie below. Scaling factors (shown in front of each element) have been applied to avoid data clustering. The detection error is smaller than the diameter of the data points (cf. Table A1).

SED
7, 1399–1446, 2015

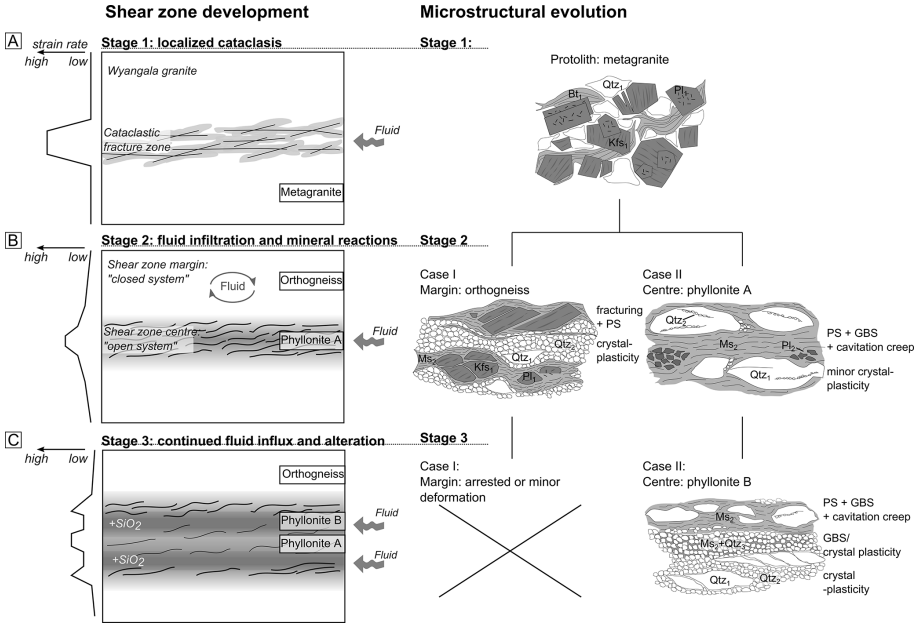

Figure 11. Schematic illustration of the temporal (Stages) and spatial (Cases) fabric development of the studied shear zone. Refer to text for details.

SED
7, 1399–1446, 2015